HHS Public Access

Author manuscript

Phys Med Biol. Author manuscript; available in PMC 2017 June 21.

Published in final edited form as:

Phys Med Biol. 2016 June 21; 61(12): 4466–4478. doi:10.1088/0031-9155/61/12/4466.

Investigation of assumptions underlying current safety guidelines on EM-induced nerve stimulation

Esra Neufeld[1], **Ioannis Vogiatzis Oikonomidis**[1,2], **Maria Ida Iacono**[3], **Leonardo M Angelone**[3], **Wolfgang Kainz**[3], and **Niels Kuster**[1,2]

[1]Foundation for Research on Information Technologies in Society (IT'IS), Zeughausstr. 43, 8004 Zurich, Switzerland [2]Swiss Federal Institute of Technology (ETH) Zurich, 8092 Zurich, Switzerland [3]Center for Devices and Radiological Health, Food and Drug Administration (FDA), Silver Spring, MD 20993, USA

Abstract

An intricate network of a variety of nerves is embedded within the complex anatomy of the human body. Although nerves are shielded from unwanted excitation, they can still be stimulated by external electromagnetic sources that induce strongly non-uniform field distributions. Current exposure safety standards designed to limit unwanted nerve stimulation are based on a series of explicit and implicit assumptions and simplifications. This paper demonstrates the applicability of functionalized anatomical phantoms with integrated coupled electromagnetic and neuronal dynamics solvers for investigating the impact of magnetic resonance exposure on nerve excitation within the full complexity of the human anatomy. The impact of neuronal dynamics models, temperature and local hot-spots, nerve trajectory and potential smoothing, anatomical inhomogeneity, and pulse duration on nerve stimulation was evaluated. As a result, multiple assumptions underlying current safety standards are questioned. It is demonstrated that coupled EM-neuronal dynamics modeling involving realistic anatomies is valuable to establish conservative safety criteria.

Keywords

EM exposure safety; coupled EM-neuronal dynamics modeling; MRI gradient coil switching; computable human phantoms; functionalized human phantoms

1. Introduction

An intricate network of nerves with varying diameters, ion-channel-dynamics, and myelination is embedded within the complex anatomy of the human body, forming the central and peripheral nervous systems. Although most nerves are well shielded within the human body from external and unintended stimulation, they can still be stimulated by

external electromagnetic sources once certain thresholds are exceeded. While intentional stimulation is used in a wide range of therapeutic applications (e.g. deep brain stimulation), unwanted stimulation can elicit responses ranging from unpleasant sensations to significant hazards, and must therefore be limited.

Magnetic resonance imaging (MRI) scanners produce strong magnetic fields, one of the strongest external exposure sources encountered by the general public. Although MRI is a powerful, non-invasive imaging modality that does not require ionizing radiation, numerous safety issues must still be considered, including interactions between electromagnetic (EM) fields and tissues, such as unintended heating by energy deposition from the RF coil (MHz range) and nerve stimulation by the switching of the gradient coils (kHz). The time varying gradient B-field induces E-fields, which lead to ionic currents across neuronal membranes, possibly resulting in the activation or inhibition of signal propagation, or synchronization of neuronal activity (Reilly and Diamant 2011b).

The IEEE (IEEE 2002) and IEC (IEC 2010) standards and guidelines define frequency-dependent thresholds for electric or magnetic field exposures, or rather dB/dt switching rates to avoid unintended adverse neuronal effects due to external sources. The underlying *E-field* limits have been identified mostly by simulations using the spatially extended nonlinear node (SENN) model (Reilly *et al* 1985, Reilly and Diamant 2011a).

The standards and guidelines are based on the following assumptions and considerations (ACs):

- AC1: the non-focality of the induced *E-field* (e.g. low spatial field gradients, no local high *E-field* spots).
- AC2: the identification of end-mode stimulation (i.e. stimulation at the neuron termination) as principal safety relevant mechanism of neurostimulation (partly consequence of the non-focality assumption). Therefore, the local *E-field* rather than its spatial gradient is deemed safety relevant.
- AC3: knowledge of local *E-field* strengths leading to neural stimulation. Typically, end-mode stimulation thresholds are determined by titration of a 20 μm SENN fiber model, which is considered conservative for peripheral nerve excitation, while a 10 μm SENN model is used for brain nerve excitation in the IEEE standard. Different thresholds are used for cardiac excitation, which have been derived from modeling and, in the case of the IEC guidelines, experimental data.
- AC4: simulations involving simplified (e.g. ellipsoidal) representations of the human body relating external stimulation strength to local *E-field* exposure. Later studies involving more complex anatomical models have not dramatically altered the predicted relationship between magnetic field exposure (Liu *et al* 2003) and local *E-field*; however, greater model detailedness and resolution result in increasing induced field predictions (So *et al* 2004).

- AC5: averaging the *E*-field over a 5 mm distance (IEEE standard) based on observations about the relationship between the stimulation threshold and the length over which the field exists (IEEE 2002).

Additional safety factors are included to account for other aspects such as threshold variations across the population and uncertainty. Further considerations allow the handling of pulse shapes deviating from sinusoidal waveforms or monophasic stimulation. The IEEE standards are intended to protect against adverse effects only (painful or aversive reactions), rather than just perceptible ones.

Some of the assumptions underlying these guidelines and standards are questionable for the following reasons:

- The complex anatomical geometry of the human body with its strongly varying dielectric property distribution and important inter-tissue contrasts make it prone to generating local *E*-field foci.
- Strongly inhomogeneous *E*-fields can potentially cause center-type (axonal) neuron stimulation (Reilly and Diamant 2011b). This becomes evident when applying the activating function concept (Rattay 1989) to tissue interfaces where the *E*-field is discontinuous, for example.
- The relationship between the induced local E-field foci and the incident field shows important inter-person variation due to differences in individual morphology. Deriving thresholds based on the switching rate or incident field strengths is therefore complicated.
- The SENN model was developed to facilitate the simulation of *E*-field-induced neurostimulation by coupling an external potential distribution to a neuronal dynamics model derived from the Frankenhaeuser-Huxley model of myelinated neurons (Frankenhauser and Huxley 1964). While the Frankenhaeuser-Huxley model has a known temperature dependence of the channel dynamics, studies using the SENN model (including those underlying the IEEE C95.6 standard) typically use the original parameters determined at 22 °C. In some studies, parameters relevant at higher temperatures have been used; however, this has been performed globally disregarding possible local temperature ‘hot-spots’. Although exposure to RF fields during MRI can lead to strong local temperature increases (in the order of 5.8 °C (Murbach *et al* 2014), and much higher for patients with impaired thermoregulation), it is unclear how this affects neuronal dynamics.
- The *E*-field thresholds derived using the SENN model were determined in a homogeneous induced *E*-field exposure. It is not clear if end-mode stimulation thresholds are altered due to inhomogeneous field distribution, as present inside the human body.
- While the SENN model was derived with the intention of creating a generic, conservative model, it is unclear how conservative it is when compared to realistic motor or sensory neuron models. Also, the SENN model does not

reproduce certain neuronal behavior (e.g. time constant, waveform dependence) observed in magnetic stimulation experiments (McRobbie and Foster 1984).

Computable, functionalized anatomical phantoms integrating coupled EM-neuronal dynamics modeling in detailed anatomical models have been developed (Neufeld *et al* 2016) and are applied here to investigate the impact of MR exposure on nerve excitation within the full complexity of the human anatomy for the first time ever. Simulation of the fields generated by a specific MRI coil system were previously performed (e.g. early work by Gandhi and Chen (1999)). Coupled EM-neuronal dynamics modeling in anatomical models has previously been used to study intentional nerve root stimulation in the spine region (Ladenbauer *et al* 2010, Laakso *et al* 2014). The goals of this paper are:

- to identify and investigate the assumptions underlying current safety standards
- to apply the computable, functionalized anatomical phantoms to MRI gradient coil switching safety evaluations by simulating neurostimulation of the sciatic nerve in a complex anatomical model
- to investigate the impact of induced *E*-field inhomogeneity due to the dielectric property variation between tissues
- to investigate the impact of local RF-induced temperature hot-spots on neuronal dynamics
- to compare the SENN model with a less generic motor-neuron model
- to examine neurostimulation mechanisms under realistic conditions.

2. Methods

The computable, functionalized anatomical human phantoms offer high fidelity and detailedness and are empowered with integrated multi-physics solvers and tissue models optimized for the simulation of physical, physiological, and biological processes in living tissue (Neufeld *et al* 2016). They are at the core of the Sim4Life simulation platform (ZMT 2015). The simulation setup consists of a functionalized computable anatomical phantom, an MRI gradient coil, and a generic RF birdcage coil (figure 1). The coupling of the different simulation steps is shown in figure 2.

2.1. Anatomical model

For the purpose of this study, the virtual population version 3.0 (ViP3.0, (Christ *et al* 2010, Gosselin *et al* 2014, IT'IS 2015)) Ella model (derived from MRI image data of a healthy, 26 year old female volunteer) was functionalized with the sciatic nerve, a large, extended nerve that is subject to inhomogeneous exposure. The sciatic nerve can be easily traced, and sophisticated, realistic neuronal dynamics models already exist for motor neurons. The nerve was segmented as part of the Ella model from the lower back to the knee, as far as discernible in the underlying image data, and a spline was placed along the nerve trajectory following the peroneal branch. Tissue material parameters were assigned based on the dielectric dispersion models from Hasgall *et al* (2014) and Laakso and Hirata (2013) and the density, thermal properties, and tissue perfusion data were based on Hasgall *et al* (2014).

2.2. Gradient coil modeling

2.2.1 Magneto-quasistatic (MQS) solver—EM simulations of the gradient coil-induced fields and currents were performed using an MQS solver. To simulate gradient coil switching, the MQS solver first calculates a magneto-static vector potential (A_0) such that the magnetic field $B = \nabla \times A_0$ satisfies the Biot-Savart law and subsequently determines the induced E-fields and currents using potential continuity while considering the inhomogeneous dielectric property distributions in the human anatomy. The equation $\nabla \cdot \sigma\nabla\phi = -j\omega\nabla \cdot (\sigma A_0)$ is solved (σ: conductivity, ω: angular frequency, ϕ: electric scalar potential) which is appropriate (Bowtell and Bowley 2000, Bossetti *et al* 2008), as ohmic currents dominate over displacement currents in the body at these frequencies. For all tissues the following conditions are satisfied: the current distribution $J \neq 0$ and $\nabla \cdot J = 0$ in the gradient coil (closed current loops), and $|\omega^2 \varepsilon d^2| \ll 1$, where d is the diameter of computational domain and $\in$ is the complex tissue permittivity, i.e. the domain is much smaller than the wavelength.

2.2.2. Simulation—The gradient coil was modeled on a z-coil (geometry and current distribution) from Jin (1998), where z is oriented along the main body axis. A residuum reduction by 10 orders of magnitude was used as convergence criterion, with a mesh of 63 million voxels and a finest resolution of 1.3 mm. The Ella anatomical model was inserted into the coil such that the center of the heart was shifted 375 mm on the z-axis from the isocenter (pelvic imaging position) and was voxeled with a 1.5 mm resolution. To scale the results from the quasistatic simulation (sinusoidal waveform) to the gradient coil switching situation, where the induced E-field and current are essentially constant during switching, the simulations were normalized to match the target slew rate (in (T m^{-1} s^{-1})). For this, the E-field was multiplied by $2\pi f$ to obtain the corresponding dB/dt. The slew rate was then determined as the average slope along the coil center line within ±20 cm from the iso-center. The following field strengths were determined (absolute values normalized to a slew rate of 100 T m^{-1} s^{-1}): the peak dB/dt (overall and in the region of the nerve), the peak E-field magnitude inside the fatty tissues (for comparison with So *et al* (2004)), the peak B_1^+ (shoulder region, B_1^+ is the circularly polarized B-field component responsible for the imaging), and the tangential E-field at the ends of the neuron model (determined by dividing the potential difference between the last two nodes by their distance).

2.3. RF-coil modeling

2.3.1. EM—The power deposition from a 16-rung ‘band pass’ 3 T RF-birdcage coil modeled on the MITS3.0 (ZMT, Zurich MedTech AG, Switzerland) (radius: 375 mm, coil height: 490 mm, shield height: 760 mm, leg width: 20 mm, ring width: 20 mm, thickness of legs and endrings: 4 mm) was determined using a hardware accelerated finite-differences time-domain (FDTD) solver employing Yee discretization (Taflove and Hagness 2005) and optimized for inhomogeneous material distributions. The coil model was tuned to the correct resonant mode by adapting the coil capacitances and validated with field measurement data. The coil was driven in quadrature mode fed by two, 90° spatially separated, ports. A two-step total-field/scattered-field approach was used, where the incident field is determined in a harmonic simulation of the empty coil with an optimized grid and then applied using

Huygens' principle to a homogeneously voxeled anatomical model (Benkler *et al* 2009). The resolution inside the anatomical model was 2.15 mm, and 60 periods were simulated (convergence tests were performed). The RF fields were normalized to a 4 W kg^{-1} wbSAR (whole body average SAR) in accordance to first level controlled operating mode (IEC 2010).

2.3.2. Thermal—Using the same discretization, the RF-induced steady-state temperature increase was determined by solving the linear Pennes bioheat equation (Pennes 1948) considering perfusion, but neglecting thermoregulation (e.g. temperature dependent perfusion and sweating). A finite-differences steady-state (FD StST) solver was used. The tissue parameters were assigned based on Hasgall *et al* (2014), Laakso and Hirata (2013). Convective boundary conditions were employed on the surface (convection coefficient $h = 6$ W m^{-2} K^{-1}, outside temperature of 25 °C) and towards internal air cavities ($h = 10$ W m^{-2} K^{-1}, cavity temperature of 37 °C) to model skin cooling and internal air flow. A Dirichlet boundary condition (37 °C) was applied to consider the local impact of large blood vessels. Neglecting thermoregulatory mechanisms such as vasodilation leads to a conservative overestimation of the temperature increase in patients with uncompromised circulatory response. In reality, the steady-state temperature is typically reached after 15–30 min of continuous exposure.

2.4. Neuronal dynamics modeling

2.4.1. Neuron models—The NEURON software (Carnevale and Hines 2006) was integrated into the computable, functionalized anatomical phantom (Neufeld *et al* 2016). Coupling of EM-fields to neurons is achieved by computing the electric potential along the neuron and using the 'extracellular mechanism' of NEURON. The novel computable phantoms also support local temperature dependent neuronal dynamics models. Such models were implemented along the sciatic nerve spline. This included a 20 μm SENN model (at 22 °C and 37 °C; called SENN22 and SENN37), a local temperature dependent SENN(T) model (Neufeld *et al* 2016), a more detailed motor-neuron model based on McIntyre *et al* (2002) (MOTOR), and a temperature dependent variant of the latter (MOTOR(T)). Since detailed motor-neuron models have only been described up to a 16 μm diameter in McIntyre *et al* (2002), a 16 μm SENN37 model (SENN37-16 μm) was also simulated for comparison.

2.4.2. Smoothing—Jittery tracing of nerve trajectories is common in image-based neuron models (evident from neuron morphologies in Hines *et al* (2004)), as the tracing process is based on stacks of image slices. Since the tangential E-field is relevant for neurostimulation, the impact of this jitter was investigated by performing simulations with the originally traced trajectory and a smoothed variant ($\vec{x}_{smooth,i} = \vec{x}_i - s(\vec{x}_i - \vec{x}_{i-1}) - s(\vec{x}_i - \vec{x}_{i+1})$, where $\vec{x}_i$ are points along the trajectory and the smoothing parameter $s = 0.1/0.2/0.3$). To investigate the impact of potential smoothing, the potenial was convoluted with Hanning windows of width 5 and 20 (equivalent to a filter length of 5/20 mm). As the IEEE standard allows for field averaing over 5 mm (IEEE 2002), simulations were also performed using a 5-point boxcar averaged potential (the node-internode distance in the 20 μm SENN model is 1 mm).

2.4.3. High field location—In addition to the placement of a neuron model along the sciatic nerve, a short SENN model segment (7 cm) was placed near the collar bone at a high *E*-field location (41V m^{-1} for a slew rate of 100 T m^{-1} s^{-1}, peak value found in fat and subcutaneous adipose tissues), to determine the external field strength at which stimulation might occur for comparison with other reported data on stimulation thresholds.

2.4.4. Pulse shape—Three time-dependent field scaling functions were used (pulse shape by which ϕ is multiplied, see figure 3):

- $f_1(t)$ is a pseudo-'biphasic' pulse with a 0.2 ms initial zero scaling interval, allowing the neuron model to equilibrate, followed by a 0.2 ms positive amplitude rectangular pulse and an equivalent negative amplitude pulse separated by a 5 ms interval. The overall simulated duration was 10 ms. This curve shape is equivalent to the shape of the derivative of the gradient coil scaling function in Turk *et al* (2012) and Bowtell and Bowley (2000), and is suitable for the modeling of gradient switching induced currents;
- $f_2(t)$ uses a single 2 ms pulse, similar to what was employed by Reilly and Diamant (2011b), to determine the rheobase;
- $f_3(t)$ uses a true biphasic pulse with a 0.2 ms initial zero scaling interval, followed by a 0.1 ms positive amplitude rectangular pulse and an equivalent negative amplitude pulse immediately after.

2.4.5. Simulations—Neuron simulations were performed:

- using the different neuron models (SENN22 / SENN37 / SENN(T) / MOTOR / MOTOR(T)),
- without smoothing / with trajectory smoothing / with potential smoothing,
- with simulation-based / with constant tangential *E*-fields (for comparison with the SENN simulations underlying the safety guidelines),
- with the three scaling functions.

3. Results

Representative visualizations of the result distributions from the EM and thermal simulations are presented in figure 4. Strong inhomogeneity is evident not only for the RF but also for the LF *E*-field. Table 1 compares the observed peak d*B*/d*t*, induced *E*, and B_1^+ values with those found by So *et al* (2004) (So *et al* (2004) specifies the values for a coil current of 1 A; for comparison purposes, they were scaled by a factor of 200, as estimated from figure 2 in So *et al* (2004), to match the 100 T m^{-1} s^{-1} slew rate). The tangential *E*-field at the ends of the neuron model was 1.9 V m^{-1}. The heating was comparable to reported steady-state peak temperature predictions (Murbach *et al* 2014), assuming fixed perfusion (absence of thermoregulation).

Sciatic nerve stimulation was observed only for a switching rate five times higher than 100 T m^{-1} s^{-1} (four times higher for the monophasic pulse $f_2(t)$, illustrating the known pulse shape

and duration dependence of the stimulation threshold and eight times higher for the truly biphasic pulse $f_3(t)$, illustrating how the rapid phase reversal can partly compensate the excitatory potential of the first phase for such short pulses). The short neuron model placed at a high field location was, however, already stimulated at 109 T m^{-1} s^{-1} (SENN22; 130 T m^{-1} s^{-1} for SENN37 and SENN(T)). Table 2 shows the change in the stimulation threshold compared to SENN22 for different temperature and smoothing models and in comparison to the MOTOR models (for the sciatic nerve stimulation with pseudo-biphasic and monophasic pulses f_1 and f_2, as well as for the short neuron model placed at a high *E*-field location). Figure 5 shows the transmembrane potential over time at four equidistantly spaced locations along the sciatic nerve (see figures 1 and 4) for a stimulation strength sufficiently high to result in spiking in all neuron models.

The chronaxie was found to be 30% lower than that obtained with homogeneous field exposure (0.12 ms, as in Reilly and Diamant (2011b)), while the threshold end-mode field strength (tangential *E*-field at neuron end obtained after titration) increased by 10%.

In comparison to the SENN37-16 μm model, the detailed motor-neuron model (MOTOR) reduced the predicted stimulation threshold by 37%, while the temperature dependent MOTOR(T) reduced it by 21%. The SENN37-16 μm model predicted a 14% higher spiking threshold than the 20 μm SENN37 model. This diameter-related increase under inhomogeneous exposure was slightly lower than the 20% expected for homogeneous exposure, where an inverse proportionality relationship between stimulation threshold and diameter holds. To ascertain that this was due to the field inhomogeneity, spiking thresholds were also determined with homogeneous exposure and straight trajectories, resulting in exactly the expected 20% difference.

4. Discussion

Although both the coil and the anatomical model differ greatly, the obtained d*B*/d*t*, *E*, and B_1^+ values (table 1) are within the same range as those observed by So *et al* (2004). The small stimulation threshold differences between Reilly's original SENN implementation and the results obtained with homogeneous exposure in this study can be explained by the different numerical approaches of the temporal neuronal dynamics integration and the different discretization of the neuron.

While temperature seems to have only a minor impact on stimulation thresholds, the action potential propagation dynamics change dramatically, as shown in figure 5. Higher temperature, global (SENN37) or local (SENN(T)), results in shorter spikes and higher (global or local) nerve conduction velocity. The temperature distribution used for the SENN(T) model was obtained neglecting perfusion upregulation by local temperature-induced vasodilation. In patients with uncompromised thermoregulation, the temperature increase hot-spot at the knee would be reduced by about a factor of two Murbach *et al* (2014) such that the neuron dynamics would be closer to that obtained using SENN37.

It is apparent in figure 5 that during gradient on-switching end-mode stimulation occurs, while during gradient off-switching axonal center-type stimulation dominates. This indicates

that contrary to common assumption center-type stimulation is similarly relevant to endmode stimulation. This has also been observed for the short SENN model placed at the high-field collar-bone location when the neuron model is placed such that the *E*-field peak is at its center. While simply terminating the dynamic neuron model by truncation is the procedure that was also applied when using the SENN model to derive the basis for the safety standards, the results must be viewed with caution, as in reality motor neurons end in neuromuscular junctions.

Changing the smoothing parameter *s* from 0 up to 0.3 results in stimulation threshold variations up to 40%, indicating that it is important to not only trace the nerve trajectory by marking the nerve location on a successive series of image slices or by placing selected points in 3D, but also to reproduce its smoothness/jaggedness and bends. Smoothing the potential increases the stimulation threshold estimation as expected (the threshold increases with widening smoothing kernel as the second potential derivative related activating function decreases). The motivation to introduce current or potential smoothing (as resulting from the 5 mm field averaging in the IEEE guidelines, AC5) is a result of strong field discontinuities observed in the simulations due to dielectric contrasts at interfaces. In reality, it is the sampling of the electric field by the finite distance between neuronal nodes that has this regularizing effect, which is correctly and naturally reproduced by discrete neuron models so that additional field smoothing is not justified. Therefore, while trajectory smoothing should be performed to avoid jaggedness and bends that are inexistent in reality, potential or field smoothing should be avoided and replaced by consideration for the finite distance between nodes. However, special attention must be paid to discretization related simulation artifacts, and removal by very local averaging can be appropriate.

The influence of field inhomogeneity on the end-mode stimulation *E*-field threshold obtained by titration indicates that it is not possible to derive stimulation field strength thresholds independent of the field distribution. As inhomogeneous fields lead to different neuron behavior, field simulations alone are insufficient and must be combined with coupled neuronal dynamics simulations, or additional safety margins need to be considered.

The short neuron segment placed at the high field location near the collar bone showed center-type stimulation starting at a switching rate of 109 T m^{-1} s^{-1} (SENN22), which is in agreement with the threshold values reported by Bowtell and Bowley (2000) and can occur in realistic imaging situations. The peak dB/dt at 100 T m^{-1} s^{-1} is close to the limit between the IEC Uncontrolled Exposure Zone and the IEC First Controlled Operating Zone for a magnetic flux density switching duration of 10 μs duration. Furthermore, considering the uncertainty associated with numerical modeling, it is concluded that the safety thresholds, which are strongly modeling-based, do not include large safety margins compared to predicted nerve stimulation (not identical with adverse or critical stimulation) thresholds.

Various assumptions underlying safety guidelines and standards appear to be problematic: The simulations indicate high spatial field gradients, conflicting with the assumption of non-focality (AC1). End-mode stimulation is not always the principal safety relevant mechanism (AC2). Therefore, and because of the impact of spatial field inhomogeneity on stimulation thresholds (AC3), local field alone is not a sufficient safety criterion. Furthermore, important

factors are overlooked by analyses based on simplified geometrical body models (AC4). The comparison with the detailed motor-neuron model indicates that the SENN model is not necessarily conservative (AC3). Consequently, the suitability of the currently applied safety thresholds must be reviewed, as enhanced safety margins might be required. Additional simulations using detailed anatomical models and, preferably, coupled neuronal dynamics modeling should be performed and experimentally validated. Our results indicate that it might be necessary to extend the standards to also account for field inhomogeneity-related factors (e.g. using approaches similar to the activating function proposed by Rattay (1989)).

As coupled EM-neuronal dynamics simulations featuring detailed anatomical models have been found to be valuable for investigating low frequency safety, functionalized anatomical models that already include neuronal dynamics models for critical nerves can significantly enhance the simulations.

5. Conclusions

Within this study, a computable, functionalized anatomical phantoms enriched with integrated neuronal dynamics solvers and tissue models, allowing coupled EM-neuronal dynamics simulations within the full anatomical complexity of the ViP3.0 models, was used to investigate low frequency exposure safety considering the combined effect of field distributions in inhomogeneous, realistic anatomies and complex neuronal dynamics. It was used to investigate assumptions underlying current safety standards. For that purpose gradient coil switching-induced sciatic nerve stimulation was studied. Aspects that were examined include: models of neuronal dynamics, impact of temperature and local hot-spots, nerve trajectory and potential smoothing, anatomical inhomogeneity, and pulse duration.

The EM simulation results are in agreement with previous publications. The results show that field inhomogeneity affects stimulation thresholds; therefore, local field strength-based limits might be insufficient and coupled EM-NEURON simulations are necessary. Realistic anatomical models are required to determine the inhomogeneous fields. Temperature has only a minor impact on the stimulation threshold, but strongly affects neuronal dynamics. While the neuron trajectory should be smoothed when performing coupled EM-NEURON simulations, the potential or E-field (AC5) along the nerve should not be. Multiple assumptions underlying the safety standards and guidelines are questioned: non-focality (AC1), the dominance of end-mode stimulation (AC2), the existence and knowledge of *E*-field stimulation thresholds (AC3), the conservativeness of SENN (SENN22 with 10/20 μm) (AC3), and the suitability of simple geometries for calculating the induced *E*-field (AC4).

The results of this study provide a valuable tool for safety assessments and stimulation mechanism investigations. The computable, functionalized anatomical human phantoms can also be used to study MR safety in the presence of implants which are expected to interact with neurons in ways that, due to the large local field gradients, cannot be captured by field thresholds only.

Acknowledgments

This study was supported by the project CAPITALIS (14930.1 PFLS-LS) of the Swiss Commission for Innovation and Technology (CTI) and FDA's Critical Path Initiative. We gratefully acknowledge J. Patrick Reilly for carefully reviewing the manuscript and providing valuable feedback.

References

Benkler, S., Chavannes, N., Kuster, N. Collection of the Joint Meeting of the Bioelectromagnetics Society and the European BioElectromagnetics Association. Davos, Switzerland: 2009. New powerful FDTD source based on huygens surface: Highly complex EM simulations performed on an ordinary PC.

Bossetti CA, Birdno MJ, Grill WM. Analysis of the quasi-static approximation for calculating potentials generated by neural stimulation. J Neural Eng. 2008; 5:44–53. [PubMed: 18310810]

Bowtell R, Bowley RM. Analytic calculations of the E-fields induced by time-varying magnetic fields generated by cylindrical gradient coils. Magn Reson Med. 2000; 44:782–90. [PubMed: 11064413]

Carnevale, NT., Hines, ML. The NEURON Book. Cambridge: Cambridge University Press; 2006.

Christ A, et al. The virtual family—development of surface-based anatomical models of two adults and two children for dosimetric simulations. Phys Med Biol. 2010; 55:N23–38. [PubMed: 20019402]

Frankenhauser B, Huxley AF. The action potential in the myelinated nerve fiber of Xenopus Laevis as computed on the basis of voltage clamp data. J Physiol. 1964; 171:302–15. [PubMed: 14191481]

Gandhi OP, Chen XB. Specific absorption rates and induced current densities for an anatomy-based model of the human for exposure to time-varying magnetic fields of MRI. Magn Reson Med. 1999; 41:816–23. [PubMed: 10332859]

Gosselin M, et al. Development of a new generation of high-resolution anatomical models for medical device evaluation: the virtual population 3.0. Phys Med Biol. 2014; 59:5287–303. [PubMed: 25144615]

Hasgall, P., Neufeld, E., Gosselin, M., Di Gennaro, F., Baumgartner, C., Klingenbock, A., Kuster, N. IT'IS database for thermal and electromagnetic parameters of biological tissues, version 2.5. 2014. www.itis.ethz.ch/database

Hines ML, Morse T, Migliore M, Carnevale NT, Shepherd GM. ModelDB: a database to support computational neuroscience. J Comput Neurosci. 2004; 17:7–11. [PubMed: 15218350]

IEC. IEC 60601-2-33, Ed. 3.0, Medical electrical equipment—particular requirements for the basic safety and essential performance of magnetic resonance equipment for medical diagnosis International Electrotechnical Commission. Geneva, Switzerland: 2010.

IEEE. C95.6-2002, IEEE Standard for Safety Levels with Respect to Human Exposure to Electromagnetic Fields. 0–3 kHz The Institute of Electrical and Electronic Engineers; New York, USA: 2002.

IT'IS. Virtual population version 3.0. 2015. www.itis.ethz.ch/virtual-population/

Jin, J. Electromagnetic Analysis and Design in Magnetic Resonance Imaging. Boca Raton, FL: CRC Press; 1998.

Laakso I, Hirata A. Computational analysis shows why transcranial alternating current stimulation induces retinal phospenes. J Neural Eng. 2013; 10:046009. [PubMed: 23813466]

Laakso I, Matsumoto H, Hirata A, Terao Y, Hanajima R, Ugawa Y. Multi-scale simulations predict responses to non-invasive nerve root stimulation. J Neural Eng. 2014; 11:056013. [PubMed: 25115613]

Ladenbauer J, Minassian K, Hofstoetter U, Dimitrijevic M, Rattay F. Stimulation of the human lumbar spinal cord with implanted and surface electrodes: a computer simulation study. IEEE Trans Neural Syst Rehabil Eng. 2010; 18:637–45. [PubMed: 21138794]

Liu F, Zhao H, Crozier S. Calculation of electric fields induced by body and head motion in high-field MRI. J Magn Reson. 2003; 161:99–107. [PubMed: 12660116]

McIntyre CC, Richardson AG, Grill WM. Modelling the excitability of mammalian nerve fibers: influence of after-potentials on the recovery cycle. J Neurophysiol. 2002; 87:995–1006. [PubMed: 11826063]

McRobbie D, Foster MA. Thresholds for biological effects of time-varying magnetic fields. Clin Phys Physiol Meas. 1984; 5:67–78. [PubMed: 6467871]

Murbach M, Neufeld E, Capstick M, Kainz W, Brunner DO, Samaras T, Pruessmann KP, Kuster N. Thermal tissue damage model analyzed for different whole-body SAR and scan durations for standard MR body coils. Magn Reson Med. 2014; 71:421–31. [PubMed: 23413107]

Neufeld E, Cassara A, Montanaro H, Kainz W, Kuster N. Functionalized anatomical models for em-neuron interaction modeling. Phys Med Biol. 2016; 61:4416–27.

Pennes HH. Analysis of tissue and arterial blood temperature in the resting human forearm. J Appl Physiol. 1948; 1:93–122. [PubMed: 18887578]

Rattay F. Analysis of models for extracellular fiber stimulation. IEEE Trans Biomed Eng. 1989; 26:676–82.

Reilly, J., Diamant, AM. Spatially extended nonlinear node (SENN) model of electrostimulation of myelinated nerve. 2011a. www.artechhouse.com/static/reslib/reilly/reilly.html

Reilly, JP., Diamant, AM. Electrostimualtion Theory, Applications, and Computational Model. Boston, MA: Artech House; 2011b.

Reilly JP, Freeman VT, Larkin WD. Sensory effects of transient electrical stimulation— evaluation with a neuroelectric model. IEEE Trans Biomed Eng. 1985; 32:1001–11. [PubMed: 4077078]

So P, Stuchly MA, Nyenhuis JA. Peripheral nerve stimulation by gradient switching fields in magnetic resonance imaging. IEEE Trans Biomed Eng. 2004; 51:1907–14. [PubMed: 15536892]

Taflove, A., Hagness, SC. Computational Electrodynamics. Boston, MA: Artech House; 2005.

Turk ES, Kopanoglu E, Guney S, Bugdayci KE, Ider YZ, Erturk VB, Atalar E. A simple analytical expression for the gradient induced potential on active implants during MRI. IEEE Trans Biomed Eng. 2012; 59:2845–51. [PubMed: 22893367]

ZMT. Sim4life version 2.0 Zurich MedTech AG. 2015. www.zurichmedtech.com/sim4life

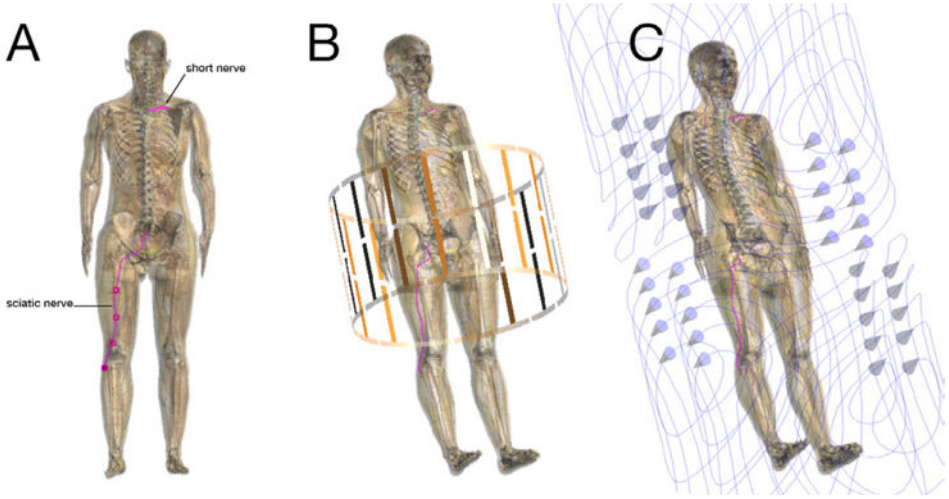

Figure 1.
Simulation setup showing the anatomical model with highlighted nerve trajectories (A), inside the RF coil (B), and inside the gradient coil (the arrows indicate the orientation of the current flow in the coil) (C).

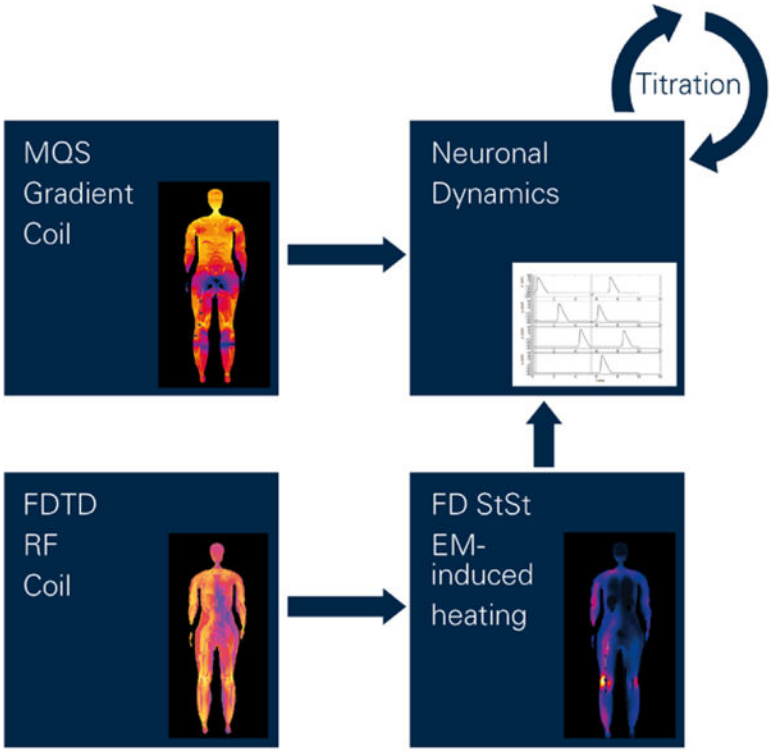

Figure 2.

Coupling of the different simulation steps: the neuronal dynamics induced by the gradient coil field is simulated with varying field magnitude (a process called ‘titration’; here a bisection approach with a threshold accuracy of 1% is used) to determine the stimulation threshold. The impact of RF-induced tissue heating can be considered.

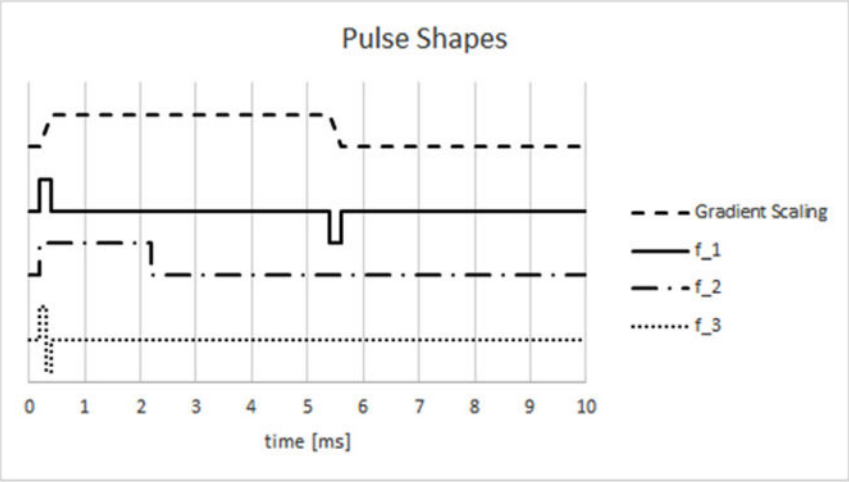

Figure 3.

Pulse shapes: pseudo-'biphasic' pulse $f_1(t)$ modeled on the derivative of the gradient coil scaling function, monophasic pulse $f_2(t)$, and true biphasic pulse $f_3(t)$.

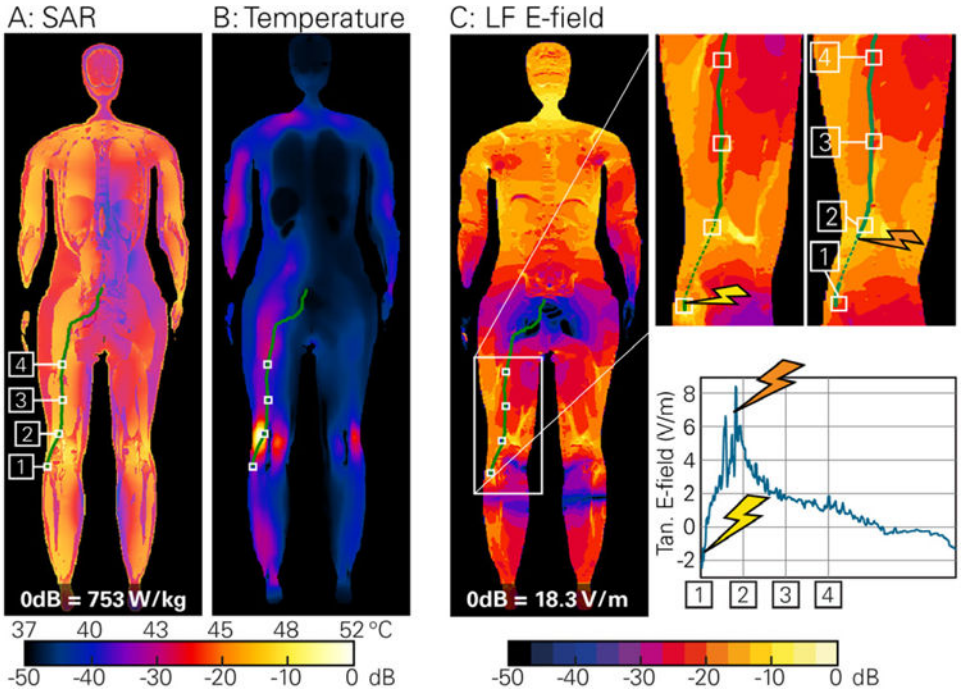

Figure 4.

Simulation results showing the local SAR distribution in dB (10 × log()) (A), the RF induced heating (B), and the LF E-field in dB (20 × log()) (C). (C) includes enlarged field distributions near stimulation locations and a plot of the tangential *E*-field along the nerve.

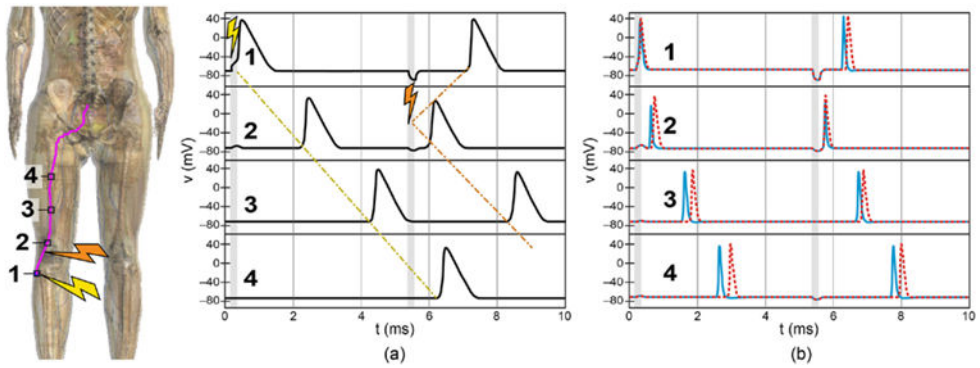

Figure 5.

Gradient coil switching transmembrane voltage over time at four equidistantly spaced locations along the sciatic nerve, for a stimulation amplitude just above the highest threshold of the three neuron models SENN22 (a), SENN37 ((b); red-dashed), and SENN(T) ((b), blue). The on-and off-switching time intervals are highlighted in grey. It is evident that both end-mode and axonal stimulation occur, and that neuronal dynamics is strongly affected by temperature.

Table 1

Comparison of field and exposure strengths obtained in this study versus values from So *et al* (2004).

	Peak d*B*/d*t*		**Peak *E*-field fatty tissue**	**Peak B_1^+**
This study	Nerve region 71 T s^{-1}	Overall 120 T s^{-1}	41 V m^{-1}	0.015 T
So *et al* (2004)		80 T s^{-1}	22–50V m^{-1}	0.0128 T

Table 2

Temperature (SENN37 and SENN(T)), nerve trajectory smoothing ($s = 0.3$), and spatial potential averaging (Boxcar averaging and Hanning window convolution) impact on thresholds; reference: SENN22.

	SENN37	SENN(T)	Nerve smooth.	Boxcar 5 mm	Hanning 5/20 mm
Pulse f_1	−19%	−13%	+40%	+35%	+19%/+92%
Pulse f_2	+4%	+16%	—	—	—
Pulse f_3	−27%	−32%	—	—	—
Short neuron	+20%	+20%	—	—	—

Note: The impact of smoothing was investigated only for the f_1 pulse.

Phys Med Biol. Author manuscript; available in PMC 2017 June 21.